

Fragment properties at the catastrophic disruption threshold: The effect of the parent body's internal structure

by

MARTIN JUTZI¹, PATRICK MICHEL², WILLY BENZ¹, DEREK C. RICHARDSON³

¹ Physikalisches Institut, University of Bern, Sidlerstrasse 5, CH-3012 Bern, Switzerland

² University of Nice-Sophia Antipolis, UMR 6202 Cassiopée/CNRS, Observatoire de la Côte d'Azur,
B.P. 4229, 06304 Nice cedex 4, France

³ Department of Astronomy, University of Maryland, College Park, MD 20742-2421, USA

TEL: (+41) 31 631 4429

FAX: (+41) 31 631 4405

E-MAIL: jutzi@space.unibe.ch

Length:

18 manuscript pages

5 Tables

19 figures

Running Title:

Fragment properties at the catastrophic disruption threshold

Corresponding author:

Martin Jutzi

Physikalisches Institut

University of Bern

Sidlerstrasse 5

CH-3012 Bern

Switzerland

TEL: (+41) 31 631 4429

FAX: (+41) 31 631 4405

E-MAIL: jutzi@space.unibe.ch

ABSTRACT

Numerical simulations of asteroid break-ups, including both the fragmentation of the parent body and the gravitational interactions between the fragments, have allowed us to reproduce successfully the main properties of asteroid families formed in different regimes of impact energy, starting from a non-porous parent body. In this paper, using the same approach, we concentrate on a single regime of impact energy, the so-called catastrophic threshold usually designated by Q_D^* , which results in the escape of half of the target's mass. Thanks to our recent implementation of a model of fragmentation of porous materials, we can characterize Q_D^* for both porous and non-porous targets with a wide range of diameters. We can then analyze the potential influence of porosity on the value of Q_D^* , and by computing the gravitational phase of the collision in the gravity regime, we can characterize the collisional outcome in terms of the fragment size and ejection speed distributions, which are the main outcome properties used by collisional models to study the evolutions of the different populations of small bodies. We also check the dependency of Q_D^* on the impact speed of the projectile.

In the strength regime, which corresponds to target sizes below a few hundreds of meters, we find that porous targets are more difficult to disrupt than non-porous ones. In the gravity regime, the outcome is controlled purely by gravity and porosity in the case of porous targets. In the case of non-porous targets, the outcome also depends on strength. Indeed, decreasing the strength of non-porous targets make them easier to disrupt in this regime, while increasing the strength of porous targets has much less influence on the value of Q_D^* . Therefore, one cannot say that non-porous targets are systematically easier or more difficult to disrupt than porous ones, as the outcome highly depends on the assumed strength values. In the gravity regime, we also confirm that the process of gravitational reaccumulation is at the origin of the largest remnant's mass in both cases. We then propose some power-law relationships between Q_D^* and both target's size and impact speed that can be used in collisional evolution models. The resulting fragment size distributions can also be reasonably fitted by a power-law whose exponent ranges between -2.2 and -2.7 for all target diameters in both cases and independently on the impact velocity (at least in the small range investigated between 3 and 5 km/s). Then, although ejection velocities in the gravity regime tend to be higher from porous targets, they remain on the same order as the ones from non-porous targets.

1 Introduction

The collisional evolution of small body populations, such as the main belt asteroids, is generally studied by using numerical models that compute the evolution of the size and velocity distributions of objects as a result of both collisional and dynamical processes. The asteroid disruption and fragmentation algorithms used in such models contain significant uncertainties. In particular, the scaling parameter is commonly defined as the critical specific impact energy Q_D^* , which results in the escape of half of the target’s mass (hence the label D for dispersal), called also the catastrophic impact energy threshold. Thus, Q_D^* is a critical function needed in all codes that include fragmentation between rocky bodies. In this paper, by numerically simulating the collisional process between small bodies, we look for the value of this catastrophic threshold as a function of the target’s diameter, internal structure, as well as impact speed, and we characterize the outcome in terms of fragment size and ejection velocity distributions. Ideally, a wide range of outcomes should be determined depending on the collisional energy (i.e. not limited to the catastrophic threshold), but this requires very massive computations that will be undertaken in further studies.

The specific impact energy is defined as $Q = 0.5m_p v_p^2 / M_t$, where m_p , v_p and M_t are the mass and speed of the projectile and the target’s mass, respectively. The catastrophic disruption threshold Q_D^* is defined as the specific impact energy leading to a largest fragment containing 50% of the original target’s mass. Up to now, some *scaling laws* have been used in collisional models to define the outcome properties of a collision. These scaling laws have been developed in order to extrapolate the results of laboratory experiments on centimeter-size targets to asteroid scales. They generally employ non-dimensional ratios involving projectile’s size, impact speed and target’s strength, and they have led to the characterization of a relationship between Q_D^* and the target’s diameter D over a wide range of values (from centimeters to several hundreds kilometers). Unfortunately, the relations derived from these scaling laws assume a uniformity of process, structural continuity and other idealizations that put their applicability into question. As a result, depending on the assumptions made, the relationships obtained between Q_D^* and D can differ over several orders of magnitude. Nevertheless, despite these discrepancies, some systematic trends arise. In particular, impacts on small objects take place in the so-called “strength-scaling” regime, where the fragmentation of an object is essentially governed by its tensile strength, whereas impacts on large asteroids take place in the “gravity-scaling” regime, where the gravity is generally assumed to control the outcome. Benz and Asphaug (1999) found that the transition between the two regimes may occur in the range of target’s diameters between 100 and 200 meters. Values of Q_D^* have been estimated using both laboratory and numerical hydrocode experiments (see recent reviews on these topics by Holsapple et al. 2002, and Asphaug et al. 2002).

The first *self consistent* study aimed at characterizing the catastrophic disruption threshold was performed by Benz and Asphaug (1999), who used a smoothed particle hydrodynamics (SPH) code to simulate the break-up of basalt and icy bodies from centimeters-scale to hundreds kilometers in diameter. Their simulations included in a simplified way the combined effects of material strength and self-gravitation, which allowed covering both the strength and the gravity regimes. However, in the latter regime, their study was still limited by the fact that the gravitational phase was not explicitly simulated; rather, an iterative procedure based on energy balance was used to identify the largest fragment formed by reaccumulation of smaller ones (see Benz and Asphaug 1999, Section 3.3 for details). Nevertheless, the mass of large fragments can be determined quite accurately using this method.

Recently, Leinhardt and Stewart (2008) started to investigate the dependency of Q_D^* on the strength of the body using the hydrocode CTH (McGlaun et al. 1990) to compute the fragmentation phase and the N -body code *pkdgrav* to compute the subsequent gravitational evolution of the fragments. They found that the value of Q_D^* can vary by up to a factor of three between strong crystalline and weak aggregates. However, they did not characterize the outcome of the disruptions at Q_D^* in terms of fragment size and velocity distributions and their model was not appropriate to address the case of porous materials.

In our study, we use an improved version of the SPH hydrocode of Benz and Asphaug (1999), which now includes a model adapted to porous materials (Jutzi et al. 2008) validated at small scales by a successful test against laboratory experiments using pumice targets (Jutzi et al. 2009a). Then, in order

to explicitly characterize the fragments produced by gravitational reaccumulation in the gravity regime, we combine it with the gravitational N -body code *pkdgrav*, as was done to reproduce asteroid families (e.g. Michel et al. 2001, 2003, Jutzi et al. 2009b). We next look for the catastrophic specific energy threshold as a function of target diameter in both the strength and gravity regime, and we determine in more detail in the gravity regime the outcome properties of the disruption as a function of the model used to characterize the target.

By explicitly accounting for the two main processes involved in large-scale collisions (fragmentation and gravitational interaction), our method allows us to determine not only the value of Q_D^* but also the full size and ejection velocity distributions of fragments down to the resolution limit imposed by the numerical techniques. Moreover, we can model different kinds of internal structure of the target and analyze the dependency of the value of Q_D^* and the fragments' properties on the target's properties. This is an important aspect since, as described for instance by Holsapple et al. (2002) and Asphaug et al. (2002), researchers developing collisional evolution codes continue to debate over which values of Q_D^* are appropriate for particular material properties, internal structures, impact speeds and object diameters. In particular, the effect of the internal structure on the outcome and on the impact energy required for disruption is a crucial information, as it constrains the collisional lifetime of the small body under consideration. It also has many implications in the framework of impact risk assessment and mitigation strategies. Indeed, it is important to make sure that a planned deflection does not lead to a disruption, and therefore the energy threshold for disruption is important information.

Here, thanks to the implementation of a model of fragmentation of porous materials, we consider two kinds of parent bodies, either non-porous or porous, which are generally believed to represent bright and dark asteroids, respectively.

In the following, we present the results of our investigations, starting in Section 2 by a description of the two kinds of target model for which we will provide the specific impact energy threshold for disruption. The numerical method is then briefly detailed in Section 3. The catastrophic disruption energy threshold of non-porous and porous targets as a function of projectile's velocity and target strengths is investigated in Section 4. The outcomes in terms of fragment size and speed distributions for both models are described in Section 5 and 6, respectively. Section 7 presents a comparison between these results allowing us to assess the sensitivity of the outcome properties and impact energy values upon the internal structure. Conclusions and perspectives are presented in Section 8.

2 Target models

The catastrophic energy threshold and corresponding fragment properties were determined for two basic models of the target's internal structure, namely non-porous and porous.

The first model consists of a purely monolithic non-porous target that initially contains only a distribution of incipient flaws and no damaged zones or macroscopic voids. Its fragmentation is computed with our SPH hydrocode (Benz and Asphaug 1994) based on a model of brittle failure of solid materials validated at small scale by comparison with laboratory experiments on basalt targets (Nakamura and Fujiwara 1991).

The second model is a porous target that consists of a body containing sub-resolution pores whose sizes are smaller than the thickness of the shock front. The fragmentation is computed using our recent model of fragmentation of porous material implemented in the SPH hydrocode and validated at small scale by comparison with laboratory experiments on pumice targets (Jutzi et al. 2008, 2009a).

The values of Q_D^* have been computed using nominal values of material parameters of basalt (non-porous targets) and pumice (porous targets). In order to investigate the influence of the tensile and shear strengths, we computed Q_D^* for two additional kinds of targets by, respectively, decreasing and increasing the tensile and shear strengths (i.e., the von Mises yield strength Y) from the nominal values. These targets are defined as weak non-porous and strong porous targets.

Then we investigated the outcome in terms of fragment size and speed distributions at Q_D^* using the nominal material properties of basalt for the non-porous targets and pumice for the porous ones. Other

material properties will be investigated in the future to determine whether our results can be generalized.

3 Numerical method

In order to characterize Q_D^* and outcome properties, we use a method and numerical codes based on the ones that have already allowed us to simulate successfully the formation of major bright-type asteroid families in different impact energy regimes (Michel et al., 2001, 2002, 2003, 2004a, b). More precisely, our method consists of dividing the process into two phases: a fragmentation phase computed by a 3D SPH hydrocode (Benz and Asphaug 1994, Jutzi et al. 2008), and a gravitational phase computed by the gravitational N-body code *pkdgrav* (Richardson et al. 2000) during which fragments can interact with each other due to their mutual attractions. In the strength regime at small scale, only the fragmentation phase needs to be computed.

Our hydrocode was originally limited to addressing the fragmentation of brittle non-porous materials. A model of fragmentation of porous bodies (that accounts for the crushing of pores in addition to the damage caused by the activation of cracks) has been developed and tested recently at laboratory scale (Jutzi et al. 2008, 2009a). In the following we give a short overview of our method and codes, and then present our simulations.

3.1 Numerical model of fragmentation

3.1.1 Classical model of brittle failure

To compute the fragmentation phase of the collision, we use a smoothed particle hydrodynamics (SPH) code. The standard gas dynamics SPH approach was extended by Benz and Asphaug (1994, 1995) to include an elastic-perfectly plastic material description (see, e.g., Libersky and Petschek 1991) and a model of brittle failure based on the one of Grady and Kipp (1980). The so-called Tillotson equation of state for basalt (Tillotson 1962) is used to relate the pressure to density and internal energy. We refer the reader to the papers by Benz and Asphaug (1994, 1995) for a detailed description of this code. This code was then used by Benz and Asphaug (1999) to make a first complete characterization of Q_D^* for basalt and ice targets at different impact speeds.

3.1.2 Model including porosity

Recently, our SPH impact code was extended to include a model adapted for porous materials (Jutzi et al., 2008, 2009a). Before presenting its main principles, we first define what is meant here by porosity. The scale of porosity must be defined in comparison with the other relevant dimensions involved in the problem, such as the size of the projectile and/or crater, etc. In particular, we define microscopic porosity as a type of porosity characterized by pores sufficiently small that their distribution can be assumed uniform and isotropic over these relevant scales. Specifically, the sizes of the pores are in this case smaller than the thickness of the shock front. In this paper, a *porous parent body* is considered to contain this kind of microporosity. Macroscopic porosity on the other hand is characterized by pores with sizes such that the medium can no longer be assumed to have homogeneous and isotropic characteristics over the scales of interest. In this case, pores have to be modeled explicitly and the hydrocode as described previously, which includes a model for non-porous brittle solids, can still be used. The presence of these large macroscopic voids will only affect the transfer efficiency and the geometry of the shock wave resulting from the impact, which can be computed using the existing code. This was done by Michel et al. (2003, 2004a) to model the disruption of pre-shattered parent bodies of S-type families. On the other hand, a body containing microporosity may be crushable: cratering on a microporous asteroid might be an event involving compaction rather than ejection (Housen et al. 1999a). Thus, for an impact into a microporous material, a part of the kinetic energy is dissipated by compaction which leads to less ejected mass and lower speeds of the ejected material. These effects cannot be reproduced by hydrocodes developed for the modeling of non-porous solids.

Our model is based on the so-called $P - \alpha$ model initially proposed by Herrmann (1969) and later modified by Carroll and Holt (1972). A detailed description of the model and its implementation in our SPH hydrocode can be found in Jutzi et al. (2008).

The original idea at the origin of the $P - \alpha$ model is based on the separation of the volume change in a porous material into two parts: the pore collapse on one hand and the compression of the material composing the matrix on the other hand. This separation can be achieved by introducing the so-called distention parameter α defined as

$$\alpha = \frac{\rho_s}{\rho} \quad (1)$$

where ρ is the density of the porous material and ρ_s is the density of the corresponding solid (matrix) material. Distention can be converted to porosity using the relation porosity = $(1 - 1/\alpha)$.

The distention parameter α is then used in the computation of the pressure and the deviatoric stress tensor. As material parameters we use those derived from our successful validation of the model by comparison with laboratory impact experiments into porous pumice (Jutzi et al., 2009a).

3.2 Numerical model of the gravitational phase

Once the collision is over and fracture ceases, the hydrodynamical simulations are stopped and intact fragments (if any) are identified. These fragments, as well as single particles and their corresponding velocity distribution, are fed into an N -body code that computes the dynamical evolution of the system to late time. Note that since the total mass is fixed, the extent of the reaccumulation is entirely determined by the velocity field imposed by the collisional physics upon the individual fragments.

Since we are dealing with a fairly large number of bodies that we want to follow over long periods of time, we use a parallel N -body hierarchical tree code (Richardson et al. 2000). The tree component of the code provides a convenient means of consolidating forces exerted by distant particles, reducing the computational cost. The parallel component divides the work evenly among available processors, adjusting the load each timestep according to the amount of work done in the previous force calculation. The code uses a straightforward second-order leapfrog scheme for the integration and computes gravity moments from tree cells to hexadecapole order. Particles are considered to be finite-sized hard spheres and collisions are identified at each step using a fast neighbor-search algorithm. The code then detects and treats collisions and mergers between particles on the basis of different options that were investigated by Michel *et al.* (2002) for monolithic non-porous parent bodies. Here we use the most realistic treatment in which a criterion based on relative speed and angular momentum is applied: fragments are allowed to merge only if their relative speed is smaller than their mutual escape speed and the resulting spin of the merged fragment is smaller than the threshold value for rotational fission. When two particles merge, they are replaced by a single spherical particle with the same momentum. Non-merging collisions are modeled as bounces between hard spheres whose post-collision velocities are determined by the amount of dissipation occurring during the collisions. The latter is determined in our simulations by the coefficients of restitution in the tangential and normal directions of the velocity vectors relative to the point of contact (see Richardson 1994 for details). The values of these coefficients are poorly constrained; we chose to set the normal coefficient of restitution to 0.3 for porous targets and 0.5 for non-porous ones, and the tangential coefficient to 1 (representing no surface friction). Michel et al. (2002) already found that values of the normal coefficient of restitution in the range 0.5-0.8 led to similar outcomes for non-porous bodies, and we checked that the same holds true in the case of porous bodies for values in the range 0.3-0.5.

Note that Richardson et al. (2009) have improved these simulations by adding a model for rigid aggregates, which allows particles to stick (or bounce) at contact and thus, grow aggregates of different shapes. Although this improvement allows a determination of shape and spins of fragments, it involves a large additional computational effort which goes beyond the scope of the present paper.

4 Simulations at the catastrophic disruption energy threshold

To characterize Q_D^* for a given impact speed, we have proceeded by trial and errors, by making several simulations and then looking for those that led to a largest fragment containing 50% of the parent body's mass. We use about 2×10^5 SPH particles to perform the simulations. In the gravity regime, in a first step, we computed explicitly the fragmentation phase by using the SPH hydrocode. We obtained a first estimate of the largest fragment mass by using the iterative procedure based on energy balance developed by Benz and Asphaug (1999). Once the impact conditions expected to lead to the appropriate remnant mass were identified, the complete simulation was carried out, this time including both the fragmentation and gravitational phases. The gravitational phase was computed using a stepsize of 50 s (several runs were made with a stepsize of 5 s and obtained similar results) and was carried out to a simulated time of 11.6 days after which the outcome does not change anymore. Note that the mass of the largest remnant found by the complete simulation (including the gravitational phase) is in a good agreement with the mass found by the iterative energy balance method (the difference is typically of the order 3-5 %).

4.1 Catastrophic impact energy threshold as a function of target diameter for non-porous and porous materials

Table 1 gives the nominal material properties of basalt and pumice used in our two models of internal structure (non-porous and porous). We define them as nominal, because in order to characterize the influence of the tensile and shear strengths, we will modify the values of these parameters to compute Q_D^* in the following subsection. Table 2 gives the impact conditions of our simulations (which, in the gravity regime, include the explicit computation of the gravitational phase) for all the investigated diameters and for the two nominal models.

Note that the largest fragment from these simulations does not contain exactly 50% of the target's mass since it would be computationally unreasonable to look for the impact conditions that lead to the exact value. To determine Q_D^* , we performed at least one additional impact simulation around the specific energy threshold and we interpolated through the corresponding values of the impact energy to derive the exact value of Q_D^* . Note that in the gravity regime, we used the mass of the largest remnant obtained by the energy balance method to perform the interpolation. In all simulations presented here, we obtained $0.35 < M_{lr}/M_{pb} < 0.65$, where M_{lr} and M_{pb} are the largest remnant and parent body masses, respectively.

Figure 1 presents the relationship between Q_D^* and target diameter for the two kinds of parent bodies and for a projectile speed of 3 km/s and impact angle of 45° (which corresponds to the most probable impact angle). As shown by Benz and Asphaug (1999) for basalt and ice targets, Q_D^* increases with increasing impact angle (and decreases with decreasing impact angle). In other words, everything else being equal, a larger projectile is needed at higher impact angle to achieve the same degree of mass loss. The same holds true for both the porous and non-porous targets investigated in this paper. The material properties of the porous target are those that provided the best match to the impact experiments on pumice targets (Jutzi et al. 2009a). Non-porous targets are characterized by material properties of basalt (Benz and Asphaug 1994), so in this case our simulations, using an improved version of the SPH hydrocode, revisit the values of Q_D^* estimated by Benz and Asphaug (1999), who used similar targets.

As expected, in the strength regime, the value of Q_D^* decreases with target diameter, while in the gravity regime, Q_D^* increases with target diameter due to the gravitational attraction that has to be overcome and that increases with the size of the target. However, in the strength regime (radius smaller than a few hundreds meters), porous targets are stronger than non-porous ones, as more energy is required to disrupt them (as found in laboratory experiments).

The opposite is true in the gravity regime, where the porous targets become weaker than non-porous ones. To explain this change of impact response we first point out that in the strength regime, the largest remnant is one large intact fragment while in the gravity regime, targets are first totally shattered by the fragmentation before building up the largest remnant through gravitational reaccumulation. One reason for the change in impact response is therefore linked to the fact that the target density of the

porous target is smaller than that of non-porous targets, leading to a less efficient reaccumulation in the porous case. We use a bulk density of 1.3 g/cm^3 for porous targets, and 2.7 g/cm^3 for non-porous ones, in order to be consistent with the estimated densities of dark-type and bright-type asteroids (e.g. Yeomans et al. 1997, Wilkison et al. 2002). Therefore, target’s masses are different for the two kinds of bodies at a given diameter. Figure 2 shows the relation between Q_D^* and mass. Compared to the relation involving sizes, the difference is not huge, but the curve for porous bodies in the gravity regime is indeed shifted toward the one for non-porous bodies. Note that the bulk density of the projectiles impacting both kinds of targets is set to 2.7 g/cm^3 . We checked in a few cases that using a projectile with a bulk density of 1.3 g/cm^3 does not lead to significantly different results than those obtained with a higher density. Another reason for the change of impact response in the gravity regime is related to the shear strength which is generally higher in non-porous targets than in porous ones. Note that while that the value of the yield strength (Y) corresponds to the shear strength in non-porous materials, this is not the case in our porous material. As described in Jutzi et al. (2008), Y is the yield strength of the matrix material and does not correspond to the "bulk" shear strength of the porous material (which is generally lower). As Leinhardt and Stewart (2008) showed, the shock wave decays more rapidly in strong (high shear strength) materials than in weak (low shear strength) materials. The authors conclude that the stronger the material, the more energy is partitioned into overcoming the shear strength. Since our porous material has a much smaller bulk shear strength than the non-porous material, more energy is partitioned into plastic deformation in the latter case. This effect could, at least partially, compensate the effect of the dissipation of energy by compression (PdV work, where P is the pressure and V is the volume) in porous targets. In section 4.5 we investigate Q_D^* for different values of the shear strength. We find that in the gravity regime, Q_D^* for non-porous targets decreases significantly with decreasing shear strength which is not the case for porous targets. The influence of the shear strength is less strong for smaller targets (in the strength regime) since in this regime, the tensile strength dominates the outcome (size of intact fragments) and, in addition, the impact energies are lower and the resulting shock waves are less strong.

We will investigate the fraction of the incoming energy which goes into dissipation by compaction, plastic deformation or kinetic energy of the target in a further study.

4.2 Influence of the impact velocity

The characterization of Q_D^* for targets of a given size involves both the size and the speed of the projectile. For a given impact speed, the projectile’s size is varied, which is what was done to produce Figs. 1 and 2. It is also important to determine the dependency of Q_D^* on the impact speed. Figures 3 and 4 show the results for the porous and non-porous targets, respectively, for impact speeds of 3 and 5 km/s in the gravity regime. In the porous case, Q_D^* is systematically higher using higher impact speed. In the non-porous case, we find that for the largest considered target size (100 km), Q_D^* becomes smaller for the higher impact speed. This change was already apparent in the results by Benz and Asphaug (1999). Stewart and Leinhardt (2008) also noticed that the slope of the Q_D^* curve at 3 km/s becomes shallower for basalt targets with large sizes and interpreted this behavior as a signature of a larger contribution of the projectile mass as it becomes a significant fraction of the target mass. However, we checked that including the projectile particles in the computation of the gravitational phase of the disruption of our 100 km-radius basalt target at both impact speeds, i.e. 3 km/s and 5 km/s did not lead to a different outcome, i.e. Q_D^* and the fragment size distributions are identical, and therefore the explanation of this change must reside elsewhere.

We also characterized Q_D^* for porous targets of 300 meters in radius using higher projectile speeds (i.e. 7 and 10 km/s, in addition to 3 and 5 km/s) and found that Q_D^* keeps increasing with the impact speed, which is consistent with the trend proposed by scaling laws (Housen and Holsapple 1990):

$$Q_D^* = C\rho R^{3\mu}V^{-3\mu+2} \quad (2)$$

where C is a constant, ρ is the density, V is the impact velocity, R is the target radius and μ is the so-called coupling parameter. Despite the fact that the considered porous target’s radius (300 meters) is

close to the transition between the strength and gravity regimes, we can still reasonably fit this scaling relationship, which is only appropriate for the gravity regime, with $\mu = 0.43 \pm 0.01$ and $C = 4.6 \pm 0.6 \times 10^{-4}$. Note that our value of μ is consistent with the values found in experiments involving porous materials (e.g. Housen and Holsapple, 1999b).

4.3 Power law scaling

For practical use by collisional evolution models, we fit (by eye) the Q_D^* curves of both kinds of targets, for the impact speeds investigated, by power laws of the form:

$$Q_D^* = Q_0 \left(\frac{R_{pb}}{1cm} \right)^a + B\rho \left(\frac{R_{pb}}{1cm} \right)^b \quad (3)$$

where R_{pb} is the radius of the parent body, ρ its density in g/cm^3 and Q_0 , B , a , b are constants to be determined. Such a functional form is often used in scaling law approaches with the two terms representing the strength and gravity regimes, respectively.

Figure 5 shows our fits for the impact speed of 3 km/s. The same kind of qualitative fit is at the origin of the values¹ given in Table 3 for the impact speed of 5 km/s. As it can be seen, we find slightly different slopes for the two materials and the two impact speeds, respectively.

4.4 Comparison with different scaling variables

Stewart and Leinhardt (2009) proposed new variables to describe catastrophic disruption. Instead of using the target diameter, they use the spherical radius of the combined projectile and target masses at a density of 1 g/cm^3 , and the critical specific impact energy is replaced by $0.5\mu V_i^2/M_T$ where μ is the reduced mass, V_i is the projectile speed and M_T is the total mass (projectile + target). Their aim was to remove ambiguities (over material density and projectile-to-target mass ratio) that are inherent in the traditional variables (Q_D^* and the target diameter). Using these new variables, they found some differences with respect to the results plotted with the traditional ones (see Stewart and Leinhardt 2009 for details). We checked whether the same holds true with our simulations, and found no difference. The reason is probably that Stewart and Leinhardt investigated an impact speed regime for which the projectile size is comparable to the target size, hence taking the projectile into account in the definition of the new variables can influence the outcome. Conversely, our simulations involve high impact speeds, and therefore smaller projectile sizes, so that using either set of variables is equal.

4.5 Influence of the tensile and shear strengths

The populations of asteroids and comets are certainly composed of a wide diversity of bodies and therefore, the parameter space of their potential material properties is probably huge. In this section, we investigate the effect of the tensile and shear strengths on the impact response of our non-porous and porous targets. To do so, we model our targets using basalt parameters for non-porous ones and pumice parameters for porous ones, but we decrease the strengths from the nominal values (Table 1) in the first case, and increase them in the second case. The new values of tensile and shear strengths are indicated in Table 4 and we define the corresponding targets as weak non-porous and strong porous targets.

As can be seen on Fig. 6, in the strength regime, the strong porous target is much more difficult to disrupt than the nominal non-porous one with identical tensile strength. On the other hand the weak non-porous target is much easier to disrupt than the nominal porous target which has again the same tensile strength. Therefore for the strength values investigated, non-porous targets are easier to disrupt in the strength regime, and the corresponding values of Q_D^* can differ by several orders of magnitude. Moreover, non-porous weak targets enter in the gravity regime at smaller sizes than their nominal counterparts, as

¹Note that we find slightly different values for the non-porous targets than the ones previously estimated by Benz and Asphaug (1999)

indicated by the earlier change of slope to a positive value of the Q_D^* curve. The reason is that for a low enough strength, gravity starts dominating at a smaller size. Conversely, the slope of the Q_D^* curve takes a positive value at larger sizes for the porous strong targets, because when the strength is high, gravity starts influencing the outcome when the size of the target is large enough to compensate from the high strength.

In the gravity regime, the dependency on strength is less dramatic, especially in the porous case for which the effect of strength is almost meaningless. In the non-porous case, the weak target is much easier to disrupt than the nominal case, in agreement with the results of Leinhardt and Stewart (2008). Moreover, the values of Q_D^* for these weak non-porous targets become smaller than for porous ones. Therefore, one cannot say that a porous target is either systematically easier or more difficult to disrupt than a non-porous one, as it depends on its strength properties and not only on porosity.

5 Outcome properties for a non-porous parent body

In this section, we analyze the outcome properties from the disruptions of our nominal non-porous targets corresponding to the impact conditions described in Table 2. In this paper, we concentrate on the gravity regime only. Although the ratios of the largest remnant to the target mass obtained from our simulations do not exactly equal 0.5, they remain close enough to 0.5 to reasonably assume that the outcome properties are still a good representation of what would occur at exactly Q_D^* . Our aim is to determine whether simple rules can be derived from the analysis of these outcome properties that could be easily implemented in a collisional evolution code. Here, we limit these properties to the fragment size and ejection velocity distributions.

Figure 7 shows the fragment size distributions obtained from the disruption of non-porous targets with different diameters. Fragment sizes are normalized by target diameters to allow a direct comparison. For all the considered target's diameters, the resulting distributions look very similar. This is a practical feature for implementation in a collisional evolution model.

We also compared the fragment size distribution from a disruption at Q_D^* using two different impact speeds. As shown on Fig. 8, there is no large sensitivity on the impact speed, at least in the considered range.

Therefore, in a collisional evolution model, it can be reasonably assumed that both the shape and slope of the fragment size distribution from the disruption of a non-porous target at Q_D^* do not depend on the target's diameter and impact speed, and thus can take one single form. For practical use by collisional evolution models, it is thus possible to characterize a reasonable fit of the fragment size distribution that is valid for all target diameters by a single power law of the form $N(> D) \propto D^\alpha$ where $N(> D)$ is the number of fragments with diameter greater than D and α is the power-law exponent. Figure 9 shows such a fit for a target of 1 km radius. We find that a value of the power-law exponent in the range between -2.2 and -2.7 can be considered to reasonably fit the size distributions for all the considered target diameters.

The analysis of the fragment ejection speeds, and in particular the average, median and largest remnant speeds, show that their values scale with the target diameter (see Fig. 10). A linear fit applies to the relationship between either the average or median speeds and the target diameter in the entire diameter range represented in a log-log plot. Another interesting property is the relationship between fragment speed and mass (Fig. 11). The same result as obtained by Michel et al. (2004a) in a different impact energy regime is found here, i.e. smaller fragments tend to have greater ejection speeds than larger ones. However, there is still a wide spread of values for fragments of a given mass, which makes it difficult to define a power-law relationship between fragment masses and speeds, such as the ones often used in collisional evolution models (see e.g., Davis 2003).

6 Outcome properties for porous parent bodies

The same simulations were performed using our nominal porous targets. The impact conditions are given in Table 2.

For all the considered target diameters, the resulting size distributions look very similar (see Fig. 12). On this plot, all the distributions essentially overlap with each other, except in a small range of sizes ($0.1 < D/D_T < 0.3$). Thus, as we did for non-porous targets, for practical use by collisional evolution models, we characterized a reasonable fit of the fragment size distributions that is valid for all target diameters with a single power law. Figure 13 shows such a fit for the target that is 1 km in radius. We find a best-fit value of the power-law exponent in the same range as for the non-porous case, between about -2.2 and -2.7 , that can be considered to reasonably describe the size distributions for all the considered target diameters.

We also characterized the fragment size distribution from a disruption at Q_D^* of a porous targets of 300 m in radius using four different impact speeds. As shown in Fig. 14, we find again that there is no large sensitivity on the impact speed, except for the highest one (10 km/s), which shows some discrepancy in the diameter range between about 0.04 km and 0.2 km. Whether this is meaningful or not will require a deeper investigation of the process at such high speeds, which we leave for future studies.

Concerning the ejection speeds, the average, median and largest remnant speeds increase with increasing target diameter (see Fig. 15).

As shown in Fig. 16, a wide spread of ejection speeds of fragments of a given mass exists. Consequently it is again difficult to define a power-law relationship between fragment masses and speeds.

7 Comparison between the outcomes for non-porous and porous targets

The analysis of the outcome properties from the disruption of non-porous and porous targets has allowed us in each case to identify some systematic behaviors, which are either independent of target size and impact speed (e.g. fragment size distribution) or scale with the target size (e.g. median and average ejection speeds). In this section, we analyze the systematic differences that can be identified and that are due to the different internal structures of the parent body. Note that we consider again only the gravity regime.

7.1 Fragment size distribution

For a given internal structure, the shape of the fragment size distribution certainly depends on the impact energy regime. For instance, in the case of a monolithic non-porous parent body, higher impact energies lead to a more continuous fragment size distribution (Michel et al. 2001, 2002, Durda et al. 2007). Moreover, Michel et al. (2003) found that the size distribution of pre-shattered non-porous targets tends to be more continuous than those of monolithic non-porous targets, for all considered target diameters. Obviously, the parameter space could not be covered exhaustively, so it cannot be guaranteed that these conclusions can be generalized. Here, at impact energies close or equal to Q_D^* , we actually find that there is not much difference between the size distributions obtained from either a non-porous target or a porous one, at least for the two materials considered (basalt and pumice). For instance, Fig. 17 shows similar size distributions obtained from the disruption of 1 km-radius porous and non-porous targets. As we indicated in previous sections, the power-law exponent that can be used to fit the size distributions is in the same range for both kinds of targets.

7.2 Ejection speeds

The average and median speeds are slightly higher for the porous targets than for the non-porous ones. This can be seen in Table 5 and in Figs. 18 and 19. As discussed in Section 4.1, this (counter intuitive)

result can probably be explained by the higher density and strength of the non-porous material. Note that these comparisons are made from simulations leading to values of M_{lr}/M_{pb} which are not exactly the same in all cases, so small differences must be interpreted with caution. Hence, we can reasonably conclude that average and median speeds are of the same order in general for both kinds of target's internal structure, although there is a systematic trend toward higher values for the porous targets.

To easily implement these results in a collisional evolution model, one can assume that the largest remnant, average and median ejection speeds scale with the target's diameter. Then, slightly greater values can be assigned to fragments from porous targets.

8 Conclusion

In this paper, we presented the results of complete simulations of disruptions that allowed the determination of the relationships between the specific impact energy threshold for disruption, called Q_D^* , and both the target diameter and its internal structure represented by porous and non-porous materials made of pumice and basalt. We confirmed the results from previous studies indicating that Q_D^* first decreases with target size in the strength regime and then increases with target size in the gravity regime. Moreover, we found that a porous body (as defined by our nominal model) requires more energy to be disrupted than its non-porous counterpart. In the gravity regime, the situation is reversed but the difference remains small. This might explain why, to first order, collisional evolution models could get away with only a single scaling law to reproduce the main characteristics of the asteroid populations (e.g. Bottke et al. 2005), despite the wide variety of internal properties that they can have.

However, by changing the nominal values of the tensile and in particular the shear strength of our targets, we found that in the gravity regime, the value of Q_D^* is not greatly influenced by the assumed strength for porous targets. Conversely, in the case of non-porous targets, the value of Q_D^* decreases significantly with decreasing strength. Therefore, in the gravity regime one cannot reasonably assume systematically that porous targets are easier or more difficult to disrupt than non-porous ones, as it depends on the assumed strengths of the latter. We plan to investigate the effect of other material properties as well as other kinds of materials in the future.

The value of Q_D^* also depends on the impact velocity and we find similar tendency as previous studies, namely an increase of Q_D^* with the impact speed. We then propose a scaling with speed for our porous targets, and find that it requires parameters that are consistent with what is expected for porous materials.

We next determined the outcome properties of the disruptions at Q_D^* , limited here to the fragment size and ejection velocity distributions in the gravity regime. We found that the size distributions keep the same qualitative aspect independent of the parent body's size and impact speed in the investigated range. For both porous and non-porous parent bodies, they can be represented by a power-law whose exponent can be used to approximate the distributions produced from all target's sizes. The average and median ejection speeds show also some systematic trends, i.e. they increase systematically with the target's diameter. Moreover, they are of the same order for both kinds of parent bodies, although slightly higher in the porous case.

These results (although limited to a particular specific impact energy) can be easily implemented in numerical algorithms aimed at studying the collisional evolutions of small body populations. They provide systematic trends in the outcome properties and scaling laws for Q_D^* , at least for the two kinds of target internal structure that we investigated, using nominal values of their material properties. Obviously, the real internal structures of small bodies cannot be limited to these two models and we plan to develop other models and use different material properties in order to study their resistance as well as the outcome properties of their disruption. While we limited our study to monolithic bodies, pre-shattered bodies and rubble piles, which may contain macroscopic voids and/or some microporosity, are likely to be present in the asteroid population. It is then essential to understand how macroscopic voids alone or combined with microporous properties as considered in this paper can influence the critical specific impact energy for disruption and whether they show some signature in the outcome properties. Then, using an improved

version of our N -body code (Richardson et al. 2009), we shall also be able to characterize the spin and shape distributions of fragments, in addition to the size and velocity distributions.

It is already clear that a deep understanding of collisions between small bodies requires the investigation of a huge parameter space. As a conclusion, there is room for a great number of studies in order to characterize the impact energies and outcome properties that will allow us to provide to collisional evolution models the different recipes that are valid for all impact conditions and kinds of real small bodies. Furthermore, this information is crucial to assess the efficiency of mitigation techniques aimed at deflecting a potential impactor with the Earth, as a first step requires a characterization of which impact conditions prevent the disruption of the body and rather permit its deflection.

Acknowledgments

This work was supported by the European Space Agency Advanced Concepts Team on the basis of the Ariadna contract 20782/07 *NEO Encounter 2029*. M.J. and W.B. acknowledge support from the Swiss National Science Foundation. P.M. acknowledges the support of the French *Programme National de Planétologie* (PNP), the French Program *Origine de Planètes et de la Vie* (OPV), and the cooperation program CNRS-JSPS 2008-2009. D.C.R. acknowledges support from the grant NNX08AM39G (NASA).

References

- Asphaug, E., Ryan, E.V., Zuber, M.T., 2002. Asteroid interiors. In: Bottke, W.F., Cellino, A., Paolicchi, P., Binzel, R.P. (Eds.), *Asteroids III*. Univ. of Arizona Press, Tucson, pp. 463-484.
- Benz, W., Asphaug, E., 1994. Impact simulations with fracture. I. Method and tests. *Icarus* 107, 98-116.
- Benz, W., and Asphaug, E., 1995. Simulations of brittle solids using smooth particle hydrodynamics. *Computer Physics Communications* 87, 253.
- Benz, W., and Asphaug, E., 1999. Catastrophic Disruptions Revisited. *Icarus* 192, 5-20.
- Bottke, W.F., Durda, D.D., Nesvorny, D., Jedicke, R., Morbidelli, A., Vokrouhlicky, D., and Levison, H. 2005. The fossilized size distribution of the main asteroid belt. *Icarus* 175, 111.
- Carroll, M.M., Holt, A.C., 1972. Suggested modification of the $P - \alpha$ model for porous materials. *J. Appl. Phys.* 43, 759-761.
- Davis, D. R. 2003. The experimental and theoretical basis for studying collisional disruption in the solar system. *Impacts on Earth*, 113.
- Durda, D.D., Bottke, W.F., Nesvorny, D., Enke, B. L., Merline, W. J., Asphaug, E., Richardson, D. C., 2007. Size-frequency distributions of fragments from SPH/ N -body simulations of asteroid impacts: Comparison with observed asteroid families. *Icarus* 186, 498.
- Grady, D.E., Kipp, M.E., 1980. Continuum modelling of explosive fracture in oil shale. *Int. J. Rock Mech. Min. Sci. & Geomech. Abstr.* 17, 147-157.
- Herrmann, W., 1969. Constitutive equation for the dynamic compaction of ductile porous materials. *J. Appl. Phys.*, 40, 2490-2499.
- Holsapple, K.A., Giblin, I., Housen, K., Nakamura, A., Ryan, E., 2002. Asteroid impacts: Laboratory experiments and scaling laws. In: Bottke, W.F., Cellino, A., Paolicchi, P., Binzel, R.P. (Eds.), *Asteroids III*. Univ. of Arizona Press, Tucson, pp. 443.

- Housen, K. R., and Holsapple, K. A., 1990. On the fragmentation of asteroids and planetary satellites. *Icarus* 84, 226-53.
- Housen, K. R., Holsapple, K. A., Voss, M. E., 1999a. Compaction as the origin of the unusual craters on the asteroid mathilde. *Nature* 402, 155-157.
- Housen, K. R., Holsapple, K. A., 1999b. Scale Effects in Strength-Dominated Collisions of Rocky Asteroids, *Icarus*, 142, pp. 21
- Jutzi, M., Benz, W., Michel, P., 2008. Numerical simulations of impacts involving porous bodies. I. Implementing sub-resolution porosity in a 3D SPH hydrocode. *Icarus* 198, 242-255.
- Jutzi, M., Michel, P., Hiraoka, K., Nakamura, A. M., Benz W., 2009a. Numerical simulations of impacts involving porous bodies: II. Comparison with laboratory experiments. *Icarus*, 201, 802-813.
- Jutzi, M., Michel, P., Benz, W., Richardson, D.C., 2009b. The formation of the Baptistina family by catastrophic disruption: porous versus non-porous parent body. *MAPS*, submitted
- Leinhardt, Z. M., Stewart, S.T., 2008. Full numerical simulations of catastrophic small body collisions. *Icarus* 199, 542-559.
- Libersky, L.D., Petschek, A.G., 1991. Smooth Particle Hydrodynamics with strength of materials. In: Trease, Fritts, Crowley (Eds.), *Proc. Next Free-Lagrange Method, Lecture Notes in Physics* 395, Springer-Verlag, Berlin, pp. 248-257.
- McGlaun, J. 1990. CTH - a three dimensional shock physics code. *Int. J. Impact Eng* 10.
- Michel, P., Benz, W., Tanga, P., Richardson, D.C., 2001. Collisions and gravitational reaccumulation: Forming asteroid families and satellites. *Science* 294, 1696-1700.
- Michel, P., Tanga, P., Benz, W., Richardson, D.C., 2002. Formation of asteroid families by catastrophic disruption: Simulations with fragmentation and gravitational reaccumulation. *Icarus* 160, 10-23.
- Michel, P., Benz, W., Richardson, D.C., 2003. Disruption of fragmented parent bodies as the origin of asteroid families. *Nature* 421, 608-611.
- Michel, P., Benz, W., Richardson, D.C., 2004a. Catastrophic disruption of pre-shattered parent bodies. *Icarus* 168, 420-432.
- Michel, P., Benz, W., Richardson, D.C., 2004b. Catastrophic disruption of asteroids and family formation: a review of numerical simulations including both fragmentation and gravitational reaccumulations. *PSS* 52, 1109-1117.
- Nakamura, A.M.; Fujiwara, A., 1991. Velocity distribution of fragments formed in a simulated collisional disruption. *Icarus* 92, 132-146.
- Richardson, D.C., 1994. Tree Code Simulations of Planetary Rings. *MNRAS* 269, 493-511.
- Richardson, D. C., Quinn, T., Stadel, J., Lake, G., 2000. Direct large-scale N-body simulations of planetesimal dynamics. *Icarus* 143, 45-59.
- Richardson D.C., Michel P., Walsh, K.J. and K.W. Flynn 2009. Numerical simulations of asteroids modelled as gravitational aggregates with cohesion. *Planetary and Space Science*, in press.
- Stewart S.T., Leinhardt Z.M. 2009. Velocity-dependent catastrophic disruption criteria for planetesimals. *Astrophys. J. Letters* 691, L133-137.
- Tillotson, J.H., 1962. Metallic equations of state for hypervelocity impact. General Atomic Report GA-3216, July 1962.

- Wilkison, S.L., Robinson, M.S., Thomas, P.C., Veverka, J., McCoy, T.J., Murchie, S.L., Prockter, L.M., Yeomans, D.K., 2002. An estimate of gross porosity and implications for internal structure. *Icarus* 155, 94-103.
- Yeomans, D.K., et al., 1997. Estimating the mass of asteroid 253 Mathilde from tracking data during the NEAR flyby. *Science* 278, 2106-2109.

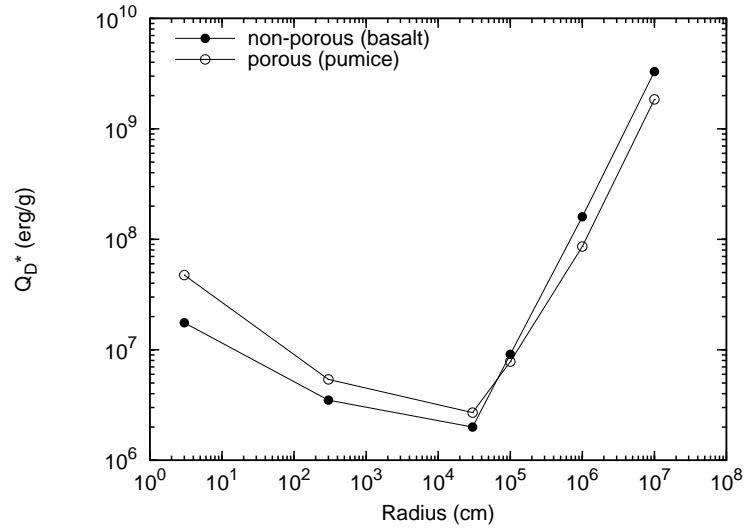


Figure 1: Catastrophic specific impact energy threshold Q_D^* (erg/g) as a function of the target radius R (cm). The impact speed and angle are 3 km/s and 45° , respectively. The internal structure of the target is either porous or non-porous, as indicated on the plot.

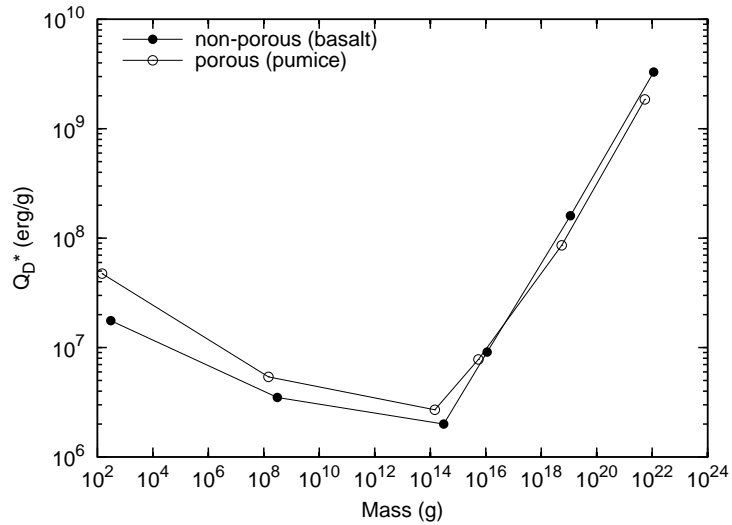


Figure 2: Catastrophic specific impact energy threshold Q_D^* (erg/g) as a function of the target mass (g). The impact speed and angle are 3 km/s and 45° , respectively. The internal structure of the target is either porous or non-porous, as indicated on the plot.

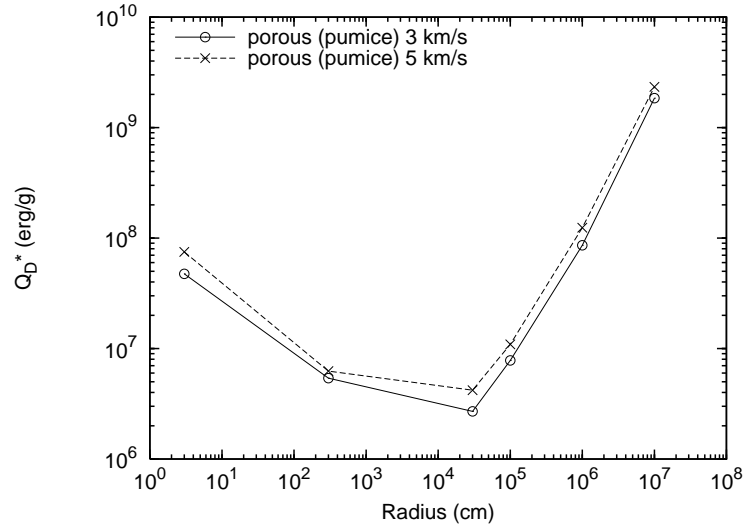


Figure 3: Catastrophic specific impact energy threshold Q_D^* (erg/g) as a function of porous target radius R (cm) for impact speeds of 3 and 5 km/s and an impact angle of 45° .

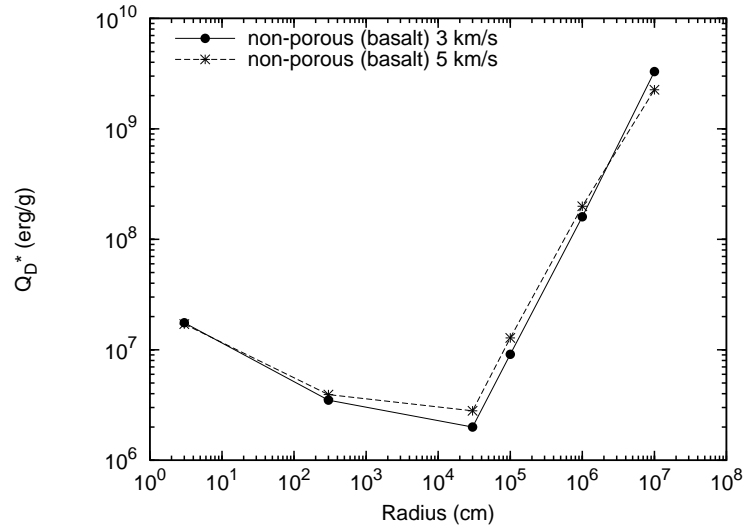


Figure 4: Catastrophic specific impact energy threshold Q_D^* (erg/g) as a function of non-porous target radius R (cm) for impact speeds of 3 and 5 km/s and an impact angle of 45° .

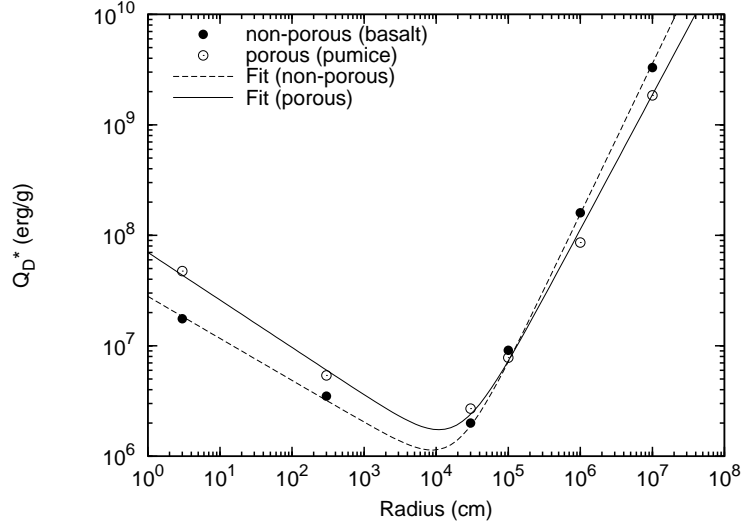


Figure 5: Fits of the catastrophic specific impact energy threshold Q_D^* (erg/g) as a function of target radius R (cm) using power laws. The impact speed is 3 km/s and the impact angle is 45° .

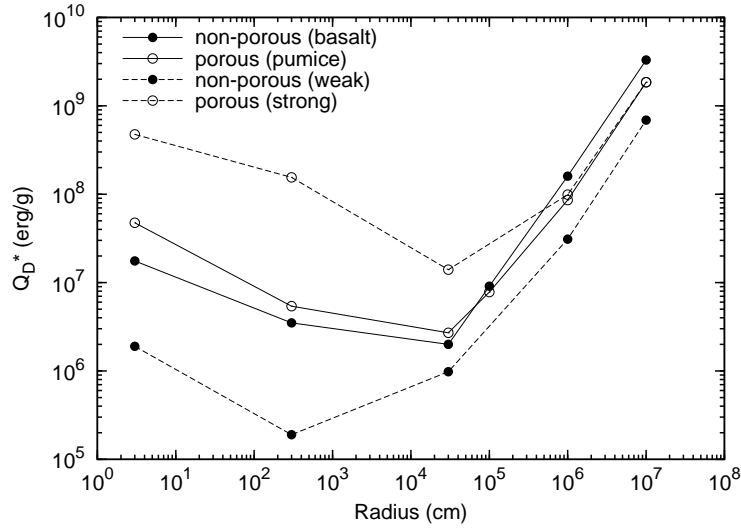


Figure 6: Catastrophic specific impact energy threshold Q_D^* (erg/g) as a function of target radius R (cm) for impact speed of 3 km/s and an impact angle of 45° . Targets are represented by basalt or pumice materials. The label weak is used for basalt non-porous targets whose tensile and shear strengths have been decreased from their nominal values, while the label strong is used for pumice porous targets whose tensile and shear strengths have been increased from their nominal values (see Tables 1 and 4).

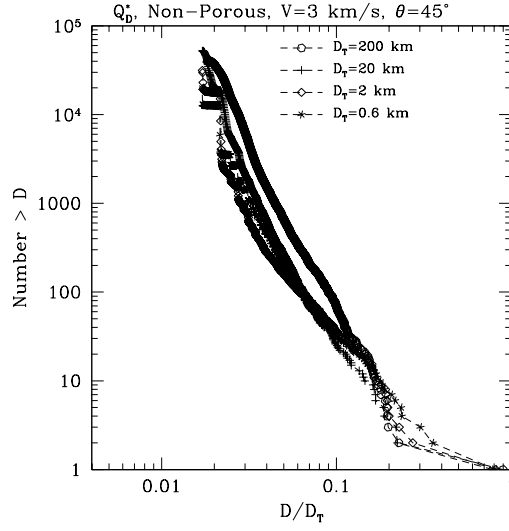


Figure 7: Cumulative diameter (km) distributions of the fragments of simulations at Q_D^* with an impact speed V of 3 km/s and an angle of impact θ of 45° . The targets are non-porous and their sizes (diameter D_T) are indicated on the plot. The fragments' diameters D are normalized to that of the target D_T , for a direct comparison.

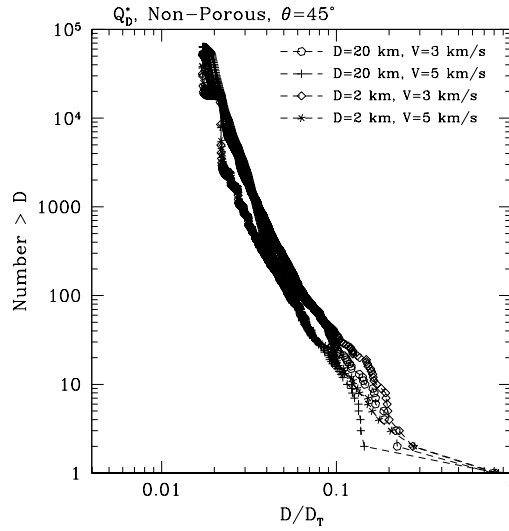


Figure 8: Cumulative diameter (km) distributions of the fragments of simulations at Q_D^* with an impact speed V of either 3 km/s or 5 km/s, and an angle of impact θ of 45° . The targets are non-porous and their sizes (diameter D_T) are indicated on the plot. The fragments' diameters D are normalized to that of the target D_T , for a direct comparison.

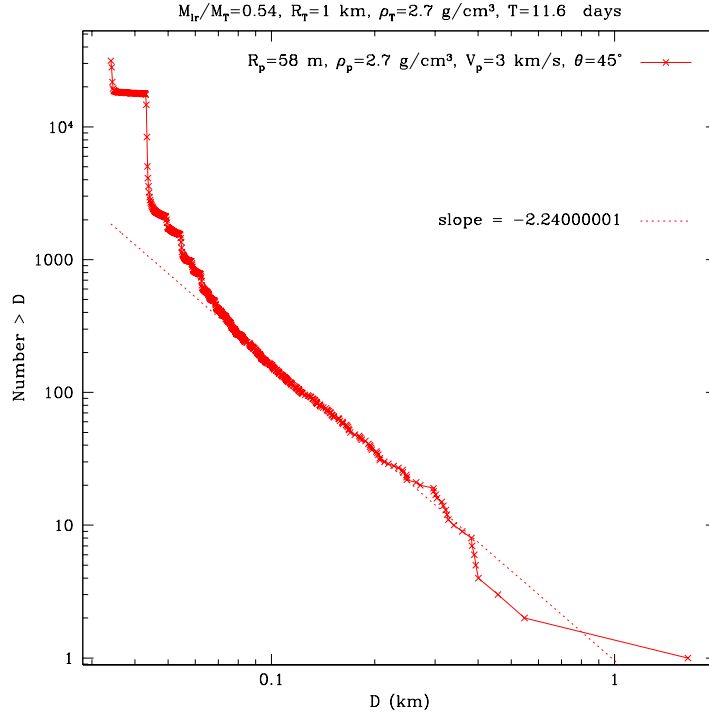


Figure 9: Cumulative diameter (km) distributions of the fragments of the simulation of disruption of the 2 km-size non-porous target at Q_D^* with an impact speed V_p of 3 km/s and an angle of impact θ of 45° . A reasonable fit to this distribution with a single slope is indicated on the plot.

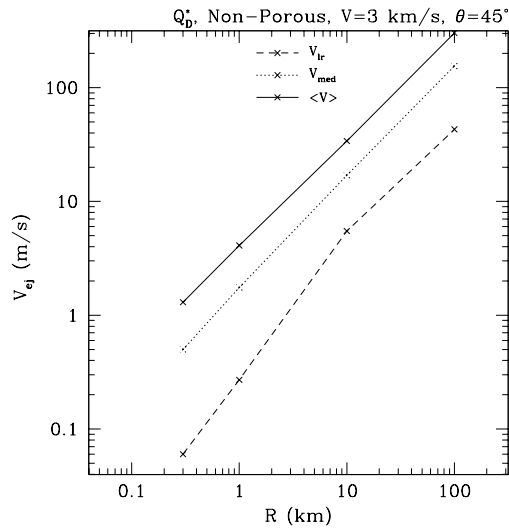


Figure 10: Different fragment ejection speeds as function of the radius R of non-porous targets, disrupted at Q_D^* with an impact speed V of 3 km/s and an impact angle θ of 45° . V_{lr} stands for the largest remnant's speed, while V_{med} and $\langle V \rangle$ are the median and average fragments' speeds, respectively.

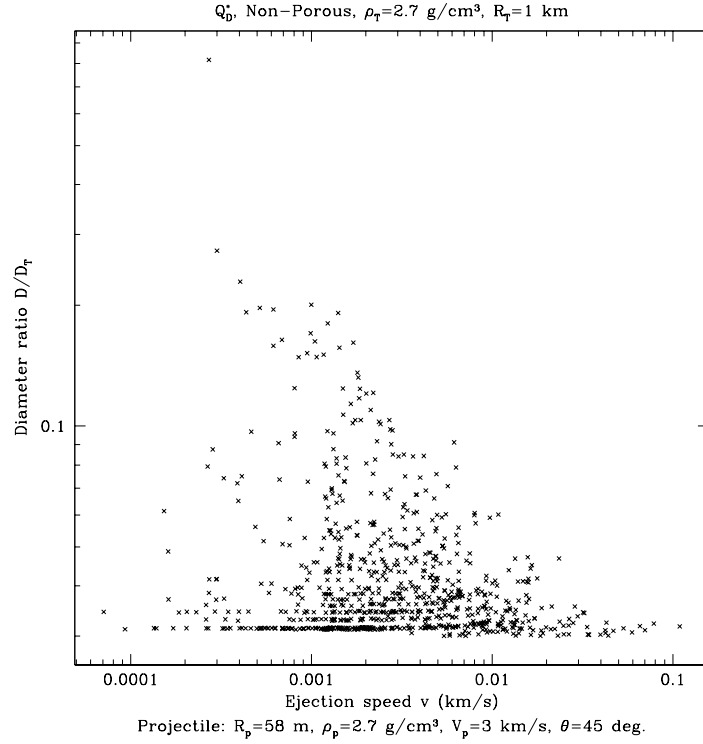


Figure 11: Fragment's diameter D (normalized to that of the parent body D_T) vs. ejection speed obtained from the breakup at Q_D^* of a non-porous target, 1 km in radius. The impact speed V_p is 3 km/s and the impact angle is $\theta = 45^\circ$. Only fragments with size above the resolution limit (i.e. those that underwent at least one reaccumulation event) are shown here.

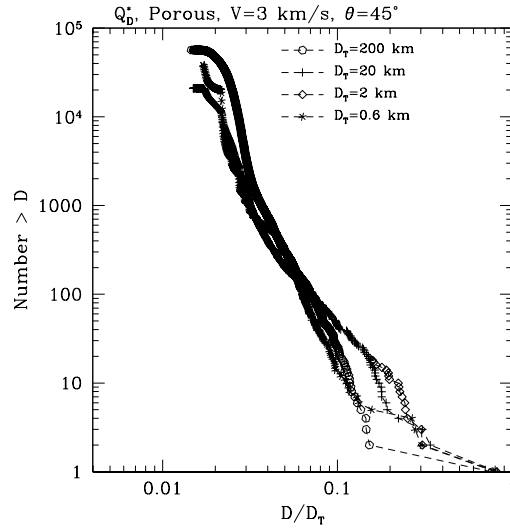


Figure 12: Same as Figure 7 for porous parent bodies.

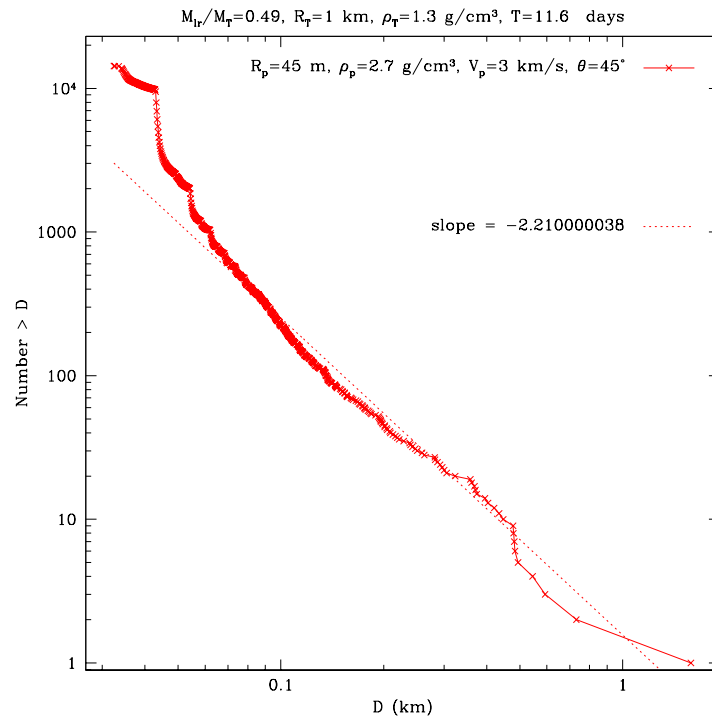


Figure 13: Cumulative diameter (km) distributions of the fragments of the simulation of disruption of the 2 km-size porous target at Q_D^* with an impact speed V_p of 3 km/s and an angle of impact θ of 45° . A reasonable fit of this distribution with a single slope is indicated on the plot.

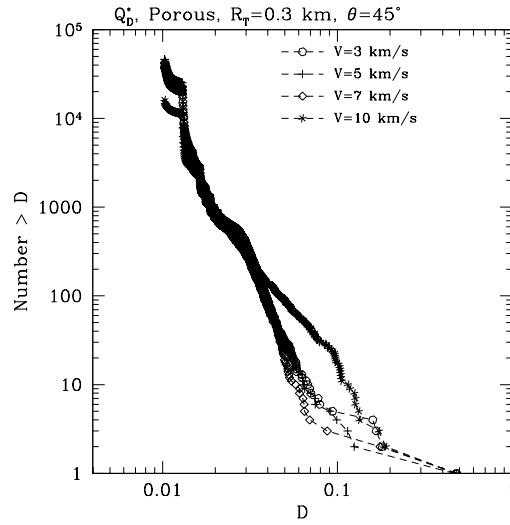


Figure 14: Cumulative diameter (km) distributions of the fragments of simulations at Q_D^* with an impact speed V of 3, 5, 7 or 10 km/s, and an angle of impact θ of 45° . The targets are porous and 300 m in radius.

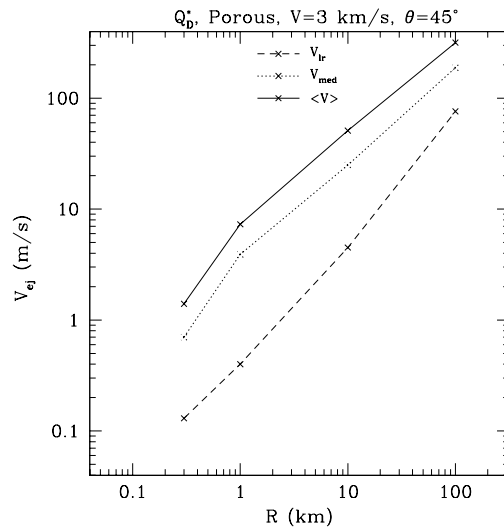


Figure 15: Same as Fig. 10 for the case of porous targets.

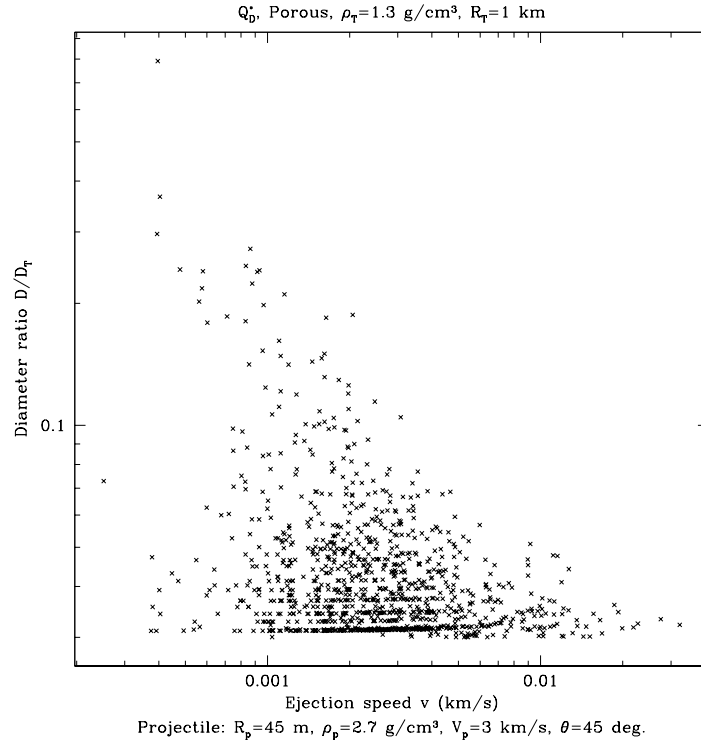


Figure 16: Fragment's diameter D (normalized to that of the parent body D_T) vs. ejection speed obtained from the breakup at Q_D^* of a porous target, 1 km in radius. The impact speed V_p is 3 km/s and the impact angle is $\theta = 45^\circ$. Only fragments with size above the resolution limit (i.e. those that underwent at least one reaccumulation event) are shown here.

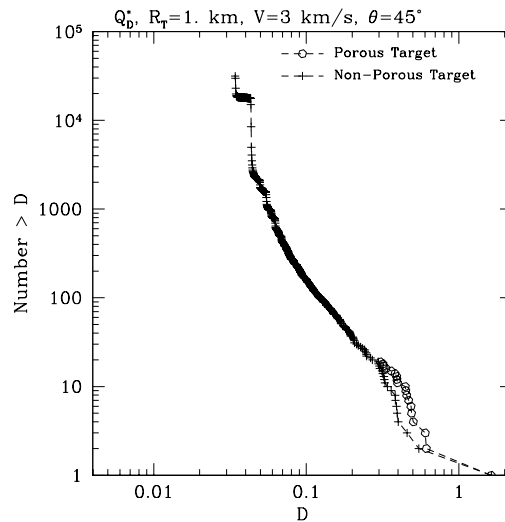


Figure 17: Comparison between the size distributions obtained from the disruption of 1 km-radius porous and non-porous targets with an impact speed V of 3 km/s and an impact angle θ of 45° .

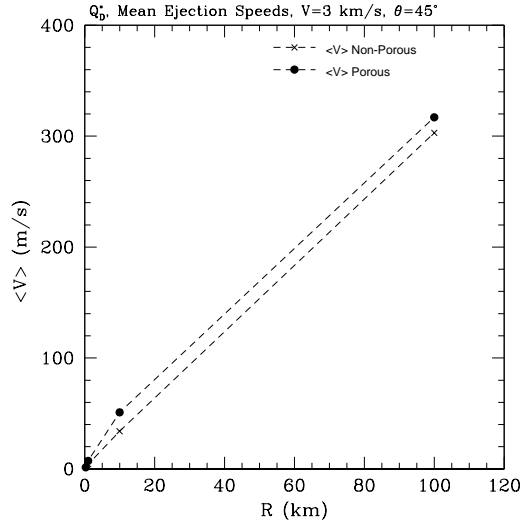


Figure 18: Mean ejection speed $\langle V \rangle$ as a function of target radius R . The impact speed V is 3 km/s and the impact angle θ is 45° . The results from the two kinds of target's internal structure are shown, as indicated on the plot.

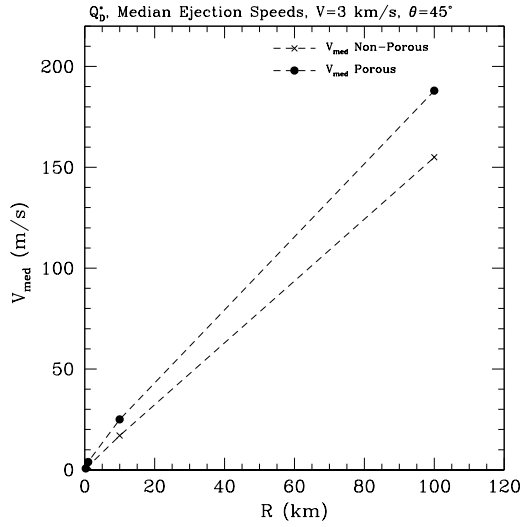


Figure 19: Median ejection speed V_{med} as a function of target radius R . The impact speed V is 3 km/s and the impact angle θ is 45° . The results from the two kinds of target's internal structure are shown, as indicated on the plot.

	Nominal Non-Porous	Nominal Porous
m	9.5	9.5
k	3.0×10^{28}	8.0×10^{37}
Y	3.5×10^{10}	3.5×10^{10}
$\sigma_T(3\text{cm})$	3.2×10^8	3.5×10^7

Table 1: Nominal material properties of non-porous and porous targets. m and k (in cm^{-3}) are the Weibull parameters used to characterize the distribution of incipient flaws. Y (in dynes/cm^2) is the yield strength, and $\sigma_T(3\text{cm})$ is the (size dependent) tensile strength (in dynes/cm^2) of a 3 cm-diameter target.

R_t (km)	Type	R_p (km)	Q (erg g^{-1})	$M_{\text{lr}}/M_{\text{pb}}$
0.00003	NP	0.0000022	1.79×10^7	0.49
0.003	NP	0.00013	3.34×10^6	0.51
0.3	NP	0.01	1.63×10^6	0.54
1.0	NP	0.058	8.38×10^6	0.54
10.0	NP	1.59	1.80×10^8	0.46
100.0	NP	41	3.10×10^9	0.50
0.00003	P	0.0000024	4.74×10^7	0.50
0.003	P	0.00011	4.49×10^6	0.63
0.3	P	0.0093	2.50×10^6	0.51
1.0	P	0.045	8.04×10^6	0.49
10.0	P	1.01	9.55×10^7	0.56
100.0	P	27.3	1.90×10^9	0.48

Table 2: Summary of simulation parameters. NP and P refer to our nominal Non-Porous and Porous targets, respectively (see Table 1). The projectile’s angle of incidence is 45° and the impact speed is 3 km/s. Impact conditions are defined by the specific impact energy $Q = (\text{projectile kinetic energy})/(\text{target mass})$, which involves the projectile’s radius R_p . $M_{\text{lr}}/M_{\text{pb}}$ is the resulting mass ratio of the largest remnant to the parent body. All simulations are aimed at being close to the catastrophic disruption threshold defined as $M_{\text{lr}}/M_{\text{pb}} = 0.5$. Note that for targets with a radius $R_t \geq 0.3$ km, the gravitational reaccumulation was explicitly simulated.

Material	v_{impact} (km/s)	Q_0 (erg/g)	B (erg cm ³ /g ²)	a	b
Porous (pumice)	3	7.0×10^7	4.15	-0.43	1.22
Porous (pumice)	5	1.0×10^8	5.70	-0.45	1.22
Non-porous (basalt)	3	2.8×10^7	0.40	-0.38	1.36
Non-porous (basalt)	5	2.9×10^7	1.50	-0.35	1.29

Table 3: Fit constants for Q_D^* (see text for details).

	Weak Non-Porous	Strong Porous
m	9.5	9.5
k	8.0×10^{37}	3.0×10^{28}
Y	1.0×10^8	3.5×10^{10}
$\sigma_T(3\text{cm})$	3.3×10^7	3.5×10^8

Table 4: Same as Table 1 for the weak non-porous and strong porous targets. Note that although the Weibull parameters of the weak non-porous targets are the same as the nominal ones of porous targets, the value of $\sigma_T(3\text{cm})$ is slightly different; the reason is that the density of non-porous targets (and therefore the volume) is higher than the density of porous ones for a similar diameter.

R_T (km)	Type	R_{min} (km)	V_r	$\langle V \rangle$	V_{med}	V_{max}
0.3	NP	0.005	0.06	1.3	0.5	888
1.0	NP	0.017	0.27	4.1	1.75	1606
10.0	NP	0.172	5.5	34	17	3789
100.0	NP	1.820	43	303	155	5562
0.3	P	0.005	0.13	1.4	0.7	216
1.0	P	0.016	0.4	7.3	3.9	695
10.0	P	0.15	4.5	51	25	2759
100.0	P	1.46	76	317	188	4876

Table 5: Properties of fragment ejection speeds. NP and P refer to Non-Porous and Porous targets, respectively. R_{min} is the radius of the smallest fragment in our simulations (all larger fragments underwent at least one reaccumulation event). Speeds are given in m/s. V_r is the largest remnant ejection speed. $\langle V \rangle$ is the average velocity of fragments which underwent at least one reaccumulation event, while V_{med} and V_{max} are, respectively, their median and maximum speed.